Fuel 359 (2024) 130478

Contents lists available at ScienceDirect

Fuel

journal homepage: www.elsevier.com/locate/fuel

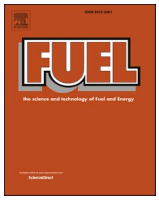

Full Length Article

A multi-layer nanocased model to explain the U-shaped evolution of shale gas permeability at constant confining pressure

Wangxing Cheng [a,b], Guanglei Cui [a,b,*], Yuling Tan [c,d], Derek Elsworth [e], Chunguang Wang [f], Chengxiang Yang [a,b], Tianyu Chen [a,b], Chuanzhong Jiang [g]

[a] Key Laboratory of Ministry of Education on Safe Mining of Deep Metal Mines, Northeastern University, Shenyang 110819, China
[b] Key Laboratory of Liaoning Province on Deep Engineering and Intelligent Technology, Northeastern University, Shenyang 110819, China
[c] Department of Engineering Mechanics, Shijiazhuang Tiedao University, Shijiazhuang 050043, China
[d] Hebei Key Laboratory of Mechanics of Intelligent Materials and Structures, Shijiazhuang Tiedao University, Shijiazhuang 050043, China
[e] Department of Energy and Mineral Engineering, G3 Center and Energy Institute, The Pennsylvania State University, University Park, PA 16802, USA
[f] College of Energy and Mining Engineering, Shandong University of Science and Technology, Qingdao 266590, China
[g] School of Engineering, The University of Western Australia, Perth, WA 6009, Australia

ARTICLE INFO

Keywords:
Global deformation
Adsorption strain
Pore heterogeneous
Permeability recovery

ABSTRACT

Understanding the evolution of shale permeability is critical in efficiently recovering gas from shale reservoirs. Two representative profiles of permeability evolution are typically experimentally observed under constant confining pressure and incremented gas pressure – "U-shape" with increasing gas pressure but sometimes absent the second upright limb of the "U" at high gas pressures. Current models fail to address these two different profiles, potentially leading to inappropriate explanation of experiment observations or inaccurate predictions of gas production. In order to determine the mechanistic reason, a multi-layer nanocased model, in which transmissive nanotubes are embedded within a cylindrical sheath of matrix, is proposed. In the model, permeability evolution is defined as a function of the evolving nanotube radius within a total matrix radius. The ensemble structure governs the transition from local deformation of the nanotube wall to the global deformation of the matrix sheath, particularly as sorbing/swelling gas gradually permeates the sheath wall. The finite element method is employed to calculate permeability evolution from an initial equilibrium state to final equilibrium. We develop a series of permeability evolution curves that match various experimental profiles. Contrasting observed permeability responses are attributed to the competition between nanotube strain and matrix global strain. The former term enlarges the nanotube radius while the latter term swells the matrix declining the permeability value. Therefore, when the matrix global strain dominates at late time, permeability decreases. Conversely, a permeability recovery stage is barely observed in the late stage because in most cases global swelling dominates the permeability evolution and an extended observational period is necessary before this swelling appears. This is also the reason why the observed final permeability ratio is rarely greater than unity. A small nanotube radius or a large adsorption strain favors a significant decrease in permeability. When the nanotubes are located within the inorganic matrix, the permeability profile conforms to poro-elastic theory and the decreasing permeability stage is barely apparent or absent. The proposed model thus provides insight into the controls on permeability evolution in shales and the controlling impact of shale matrix properties by considering the inhomogeneities of the shale matrix.

1. Introduction

Due to their massive reserves, shale gas reservoirs play a critical role in modern energy supply [1]. The coupling and high sensitivity of fluid flow to reservoir deformation makes the process of exploiting shale gas a complex phenomenon [2]. Because of their highly heterogeneous pore structure, dual-porous characterizations are extensively employed in describing the multi-scaled gas flow process in reservoirs [3]. As a result, permeability – which serves as the key parameter that links the coupling process and controls gas flow characteristics – has been investigated

* Corresponding author at: Key Laboratory of Ministry of Education on Safe Mining of Deep Metal Mines, Northeastern University, Shenyang 110819, China.
E-mail address: cuiguanglei321@163.com (G. Cui).

https://doi.org/10.1016/j.fuel.2023.130478
Received 4 October 2023; Received in revised form 12 November 2023; Accepted 22 November 2023
Available online 30 November 2023

both experimentally and theoretically [4,5]. However, experimental observations are not fully reconciled as the impact of pore inhomogeneity has yet to be fully addressed.

Typical boundary conditions comprising constant confining pressure are generally assumed in both experimental and theoretical treatments [6,7] for a number of reasons. First, (i) shale reservoirs are usually horizontally distributed and the overburden stress remains invariant (Fig. 1(a)) during gas depletion [8]. Second, (ii) constant confining pressures are readily replicated in the laboratory. In this condition, the confining pressure is retained as a constant total stress with gas pressure increasing/decreasing to represent permeability evolution during the gas injection/depletion process [9,10]. However, experimental observations record a spectrum of responses, as illustrated in Fig. 1 (b). In most cases, permeability decreases with increasing gas pressure as a result of sorption [11,12]. However, permeability may also first decrease and then recover slightly with increasing gas pressure [13,14] with this response being apparent for both sorbing (i.e. N_2, CH_4, and C_2H_6) and non-sorbing (i.e. He and Ar) gases [15].

The concept of apparent permeability has been adopted to explain the observation that the early decrease in permeability [16] as continuous flow theory [3] may no longer be valid in the shale matrix due to the much smaller pore diameter of the shale. Apparent permeability is usually defined by a combination of the slippage factor and intrinsic permeability [17]. The first term is directly related to the Knudsen number, (K_n), which is a function of gas pressure [4] and pore diameter [18], while the second term is determined by effective stress. In early work, the slippage factor, $f(K_n)$, was defined in terms of a Klinkenberg correction of $1 + b_k/p$, with b_k obtained from fitting against experimental results [18]. In contemporary views, $f(K_n)$ may be obtained theoretically [19,20]. For shale gas reservoirs the concept of apparent permeability was first introduced in 2007 [21] to describe gas flow in the shale matrix and to correct for slip velocities that are inversely proportional to gas pressure [22]. These concepts have been used to explain the observed behaviour of early permeability decreases [23] and to also accommodate gas adsorption [24]. Such slippage effects are only significant at low gas pressures (<5 MPa) [25] due to its inverse proportionality to pressure. Therefore, permeability rebounds at higher gas pressures cannot be explained by this current concept of apparent permeability [15].

More recently, poro-elasticity has been utilized to rationalize the enigmatic response of permeability evolution to gas pressures. In this approach, permeability is related to effective stress and increases during the gas injection as effective stresses decrease [26,27] with adsorptive behaviour considered as a mechanism to explain early decreases in permeability [28]. Within this framework, decreases in permeability are attributed to gas adsorption, while later stage increases are attributed to decreases in effective stress as pressure builds as sorption and related swelling reaches a maximum. The transition from local to global behaviour may also be invoked to control permeability evolution [29,30]. In this, during early gas injection, permeability behaviour is dominated by local behaviour, with the swelling of the matrix adjacent to the fracture reducing permeability. Global behaviour only controls permeability evolution at later stages where the global swelling increases permeability [31,32]. Furthermore, the concept of internal swelling has been introduced to better describe the impact of internal and external swelling [19–22] and several permeability models [33–36] have been proposed in replicating permeability evolution under constant confining pressure. In these models, the ultimate equilibrium permeability is usually larger than the original value, which is seldom observed in the experiment.

For both apparent permeability and poro-elastic approaches, pore structure characteristics and heterogeneity are seldom considered. Scanning electron microscopy (SEM) [37] and transmission electron microscopy (TEM) [38] imaging (Fig. 1 (c)) indicate substantial heterogeneity in the shale matrix with both organic and inorganic matter [39]. Both the larger-sized pores of various geometries and the smaller nanotubular pores are present in the inorganic matrix [40–44]. The organic matter can be further sub-divided into nanotube pores within kerogen. The form of gas storage varies with the pore type – that is, gas is adsorbed on the surface of the organic pores and only remains in the free state in the inorganic pores [2,7]. This disparity certainly impacts permeability evolution yet has seldom been accommodated in previous approaches.

In summary, shale matrix comprises inorganic minerals and embedded organic matter with both mechanical and gas transport properties exhibiting strong diversity as a result of this heterogeneity

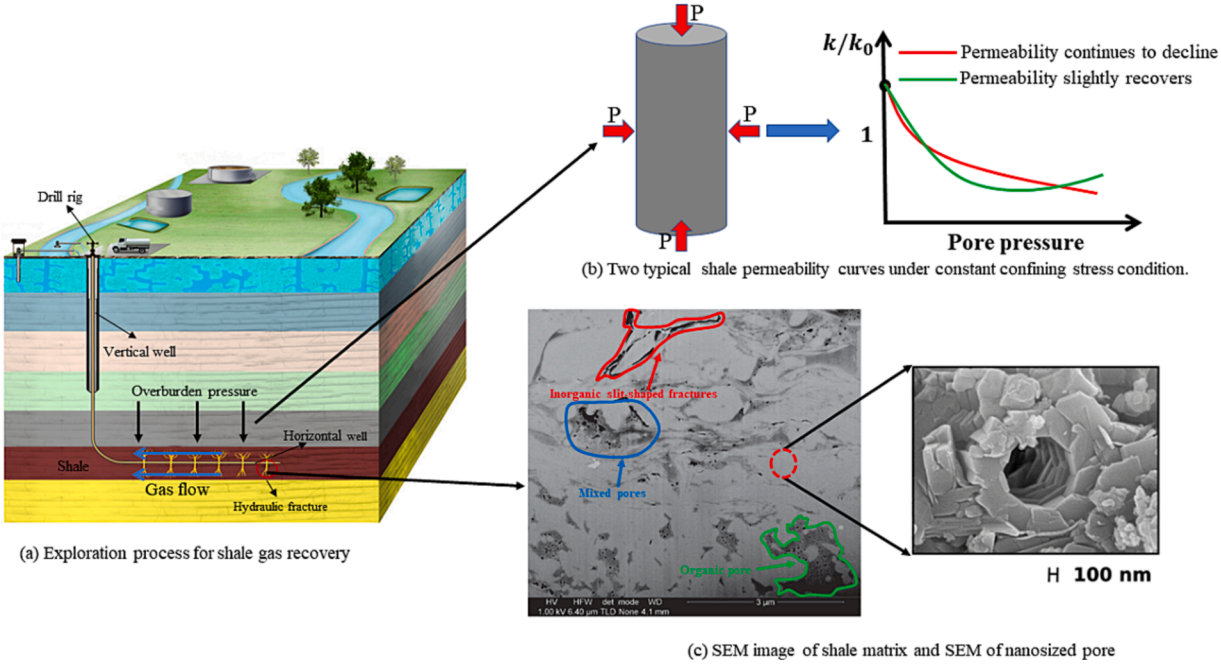

Fig. 1. (a): Exploration process for shale gas recovery, (b) Two typical shale permeability curves under constant confining stress condition, and (c) SEM image of shale matrix and SEM of nanosized pores [45–48].

[7,13]. Existing literature [11,15] shows different evolutionary patterns of permeability including both monotonic decline with increasing gas pressure and also rebound. The following presents a consistent model to explain and characterize these enigmatic phenomena. We develop a coupled multi-layer nanocased model to represent the geometry of the shale as well as its associated mechanical and transport properties. Inhomogeneities in pore structure are accommodated in the model with numerical simulation results validated against experimental data and parameter sensitivity studies conducted. These details are reported in the following.

2. Conceptual model

Shale reservoirs are generally described as dual-porous media that comprise matrix (i.e. organic matter and inorganic matter) and fractures (i.e. nanotubes) [7]. The gas is mainly stored (i) in a free state in the nanotubes and (ii) as an adsorbed or dissolved state in the matrix [2]. The microscopic observation suggested that the pores within the shale matrix are primarily nanopores taking about 80 % of the whole pore volume [43,44]. As the main flow conduit for the gas, the nanotubes directly determine the evolution of the overall permeability with this response dominated by variations in their aperture [7]. The pores and specific surface area that exists in the matrix system provide gas storage. The process of gas flow is accompanied by changes in pore pressure that alter nanotube radius/aperture and therefore impact permeability evolution. These changes are inextricably linked to external boundary conditions. Thus, we consider – in particular – the processes of gas adsorption under a specific boundary condition (i.e. constant confining pressure). We additionally focus on the relationship between nanotube strain, volume strain (matrix global strain), nanotube radius/aperture, and permeability.

2.1. Nanotube strain and volume strain

The porosity and permeability of the nanoporous medium are primarily controlled by the radii/apertures of the nanotubes. To analyse controls on nanotube radius/aperture, we consider a representative elemental volume (REV) in the dual porous medium as an example with nanotube strain and volume strain of the shale are defined as [49]:

$$\varepsilon_{ns} = 2\frac{\Delta rn}{r_{n0}} + \left(\frac{\Delta rn}{r_{n0}}\right)^2 \tag{1}$$

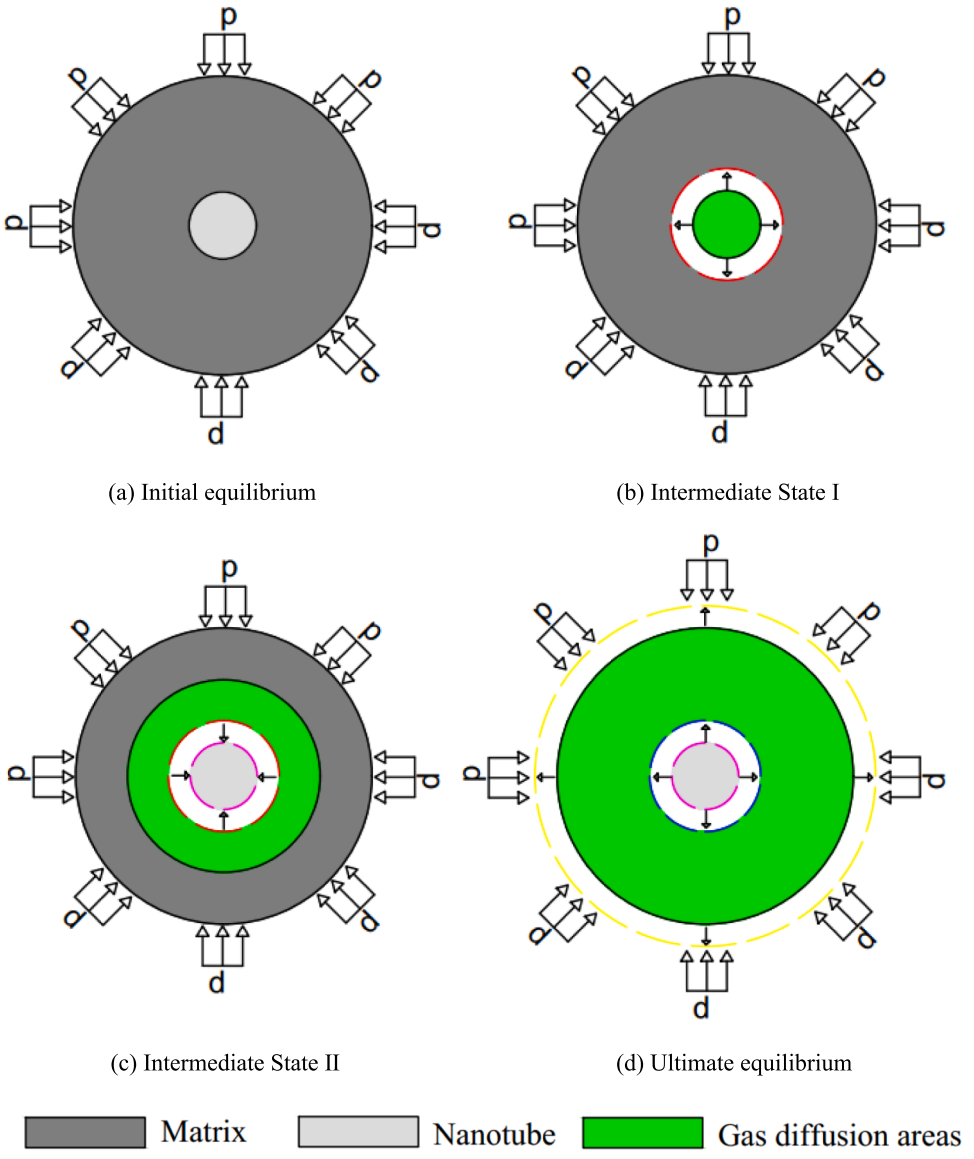

Fig. 2. The deformation of matrix-nanotube component during gas injection process under constant stress condition.

$$\varepsilon_{vs} = 2\frac{\Delta rm}{rm0} + \left(\frac{\Delta rm}{r_{m0}}\right)^2 \quad (2)$$

where ε_{ns} and ε_{vs} are the nanotube strain and volume strain of the shale, respectively, r_n and r_m are the radius of the nanotube and surrounding matrix, respectively, where Δ denotes the variation of the variable and the subscript 0 denotes the initial value.

2.2. Gas injection process under constant confining pressure

The transition from local to global deformation under constant confining pressure condition is examined by injecting adsorbed gas (e.g. CH_4), as shown in Fig. 2. The evolution of shale permeability is a relative deformation process due to differences in the mechanical properties of the matrix and nanotubes. In this work, the concept of 'local' and 'global' are defined based on the gas diffusion area – the former referring to the condition where gas molecules are concentrated upon nanotube, and the later with gas occupying most part of shale matrix under global condition. Meanwhile, the concept of nanotube strain and matrix strain are defined according to the deformed body.

Before injection, the shale is in static equilibrium with no interaction between the matrix–nanotube system, as shown in Fig. 2 (a). With injection, the gas pressure in the nanotube increases rapidly and propagates the full length of the nanotube, with a minimal pressure drop between inlet and outlet, but is contained within the pore/tube. As a result, local strain causes the nanotube to swell and thus compresses the matrix, as shown in Fig. 2 (b). During this stage, the nanotube dilates but the volume strain is zero and localised to the nanotube. As gas diffuses from the nanotube into the matrix, the local strain in the matrix (nanotube wall) increases due to both gas adsorption and increased matrix pressure. Under this condition, the matrix swells while the nanotube wall is compressed, as shown in Fig. 2 (c). This process occurs in a localised area near the nanotube wall and the nanotube strain begins to decrease while the volume strain on the exterior of the pore casing (r_m) remains constant. As the gas diffuses further into the matrix, the gas pressure propagates into the matrix until a new equilibrium state is reached. During this process, the volume strain in the control volume begins to increase due to both the increasing gas pressure in the matrix and the swelling volume/area subject to gas adsorption. As this occurs throughout the matrix while the confining pressure remains constant, both the matrix and the nanotube swell, as shown in Fig. 2 (d). The matrix exhibits both inward and outward swelling characteristic after gas adsorption. Internal swelling, facilitated by easily deformable nanotube, compresses the nanotube and reduce the permeability value. Simultaneously, outward swelling due to constant confining pressure, promotes volume expansion and expands nanotube. The compression and expansion behavior of nanotubes can be regarded as indicative of specific stages in the gas diffusion process within the matrix. Specifically, the compression of nanotubes corresponds to the second stage, characterized by a decline in permeability, whereas the swelling of nanotubes aligns with the third stage, marked by either a further decline in permeability or a potential recovery.

As a consequence, shale permeability evolves through three distinct phases (Fig. 3) and with two distinct overall trends. In the first stage (i.e. the increasing stage), the increase in permeability is caused as the gas immediately fills the nanotube under pressure at the beginning of the gas injection phase. The displacement of the nanotube wall increases and the nanotube dilates, thereby resulting in matrix compression and an increase in both nanotube radius/aperture and permeability. In the second stage (i.e. the decreasing stage), the decrease in permeability is caused by gas diffusion and adsorption into the matrix, which increases the matrix pressure and results in both the swelling of the matrix and the complementary shrinking/closure of the nanotube. In the third stage (i.e. increasing or decreasing permeability), the increasing and outwardly migrating volumes affected by gas pressure and adsorption result in an increasing volume strain in the matrix with global swelling resulting in an increase in nanotube aperture. During the second stage, the primary influencing factor is the expansion of the matrix, exerting compression on the nanotubes. In the subsequent third stage, the evolution of permeability is chiefly governed by the intricate interplay between the global expansion of the matrix and the concurrent expansion of the nanotubes.

3. Mathematical model

Mass transport of gas and resulting stress transfer between the nanotube and the matrix system result in changes in nanotube aperture/radius and hence permeability of the porous medium during the gas

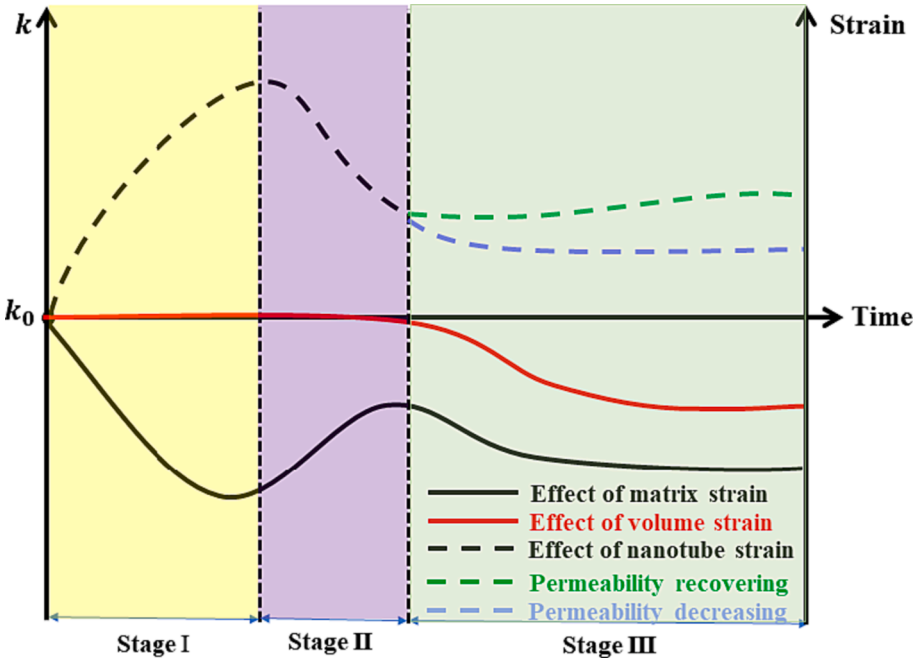

Fig. 3. Evolution of shale permeability under constant confining pressure.

injection. We represent these changes through a set of partial differential equations (PDEs) to define these interactions and link the resulting variations in internal strain with permeability.

3.1. Reservoir deformation

For a poro-elastic medium, the governing equations for mechanical deformation of the matrix and the nanotube are defined as [50]:

$$Gu_{i,kk}+\frac{G}{1-2v}u_{k,ki}-\alpha_m p_{m,i}-K\varepsilon_{s,i}+f_{mi}=0 \tag{3}$$

$$Gu_{i,kk}+\frac{G}{1-2v}u_{k,ki}-\alpha_n p_{n,i}+f_{ni}=0 \tag{4}$$

where $G=E/2(1+\nu)$, $K=E/3(1–2\nu)$, K is the bulk modulus, Pa, G is the shear modulus, Pa, E is the Young's modulus, Pa, ν is the Poisson's ratio, α is the Biot coefficient and p is the gas pressure, Pa. Subscripts m and n denote the matrix and nanotube, respectively. f_{mi} and f_{ni} represent the interaction force between the two components, with $f_{mi}+f_{ni}=0$, and ε_s is the sorption-induced volumetric strain, usually expressed by a Langmuir-type equation [51]:

$$\varepsilon_s=\frac{\varepsilon_L p}{p+p_L} \tag{5}$$

where ε_L is a constant that represents the volumetric strain at infinite pore pressure and P_L is the Langmuir pressure constant that represents the pore pressure at which the measured volumetric strain is equal to $0.5\varepsilon_L$. Eqs. (3) and (4) are the general form of the governing equation for the deformation of the matrix and the nanotube, with the gas pressure recovered from the gas flow equation listed below.

3.2. Gas flow in the reservoir

In this study, the gas in the nanotube is treated as free gas while the gas on the inorganic and in the kerogen is treated as adsorbed gas. For free gas, the flow regimes are distinguished by the Knudsen number. The Knudsen number, Kn, defined as the ratio of the molecular mean free path to the pore diameter, is a widely recognized dimensionless parameter determining the degree of appropriateness of the continuum flow model. For the free gas in the nanotube, whose diameter is 10~100 nm, the flow regime is also one of slip flow. The absorbed gases are transported due to the concentration gradient. A Langmuir model is used to define the adsorption process while the gas flow in the kerogen and the inorganic is defined by diffusion. Gas transport in porous media usually involves two mechanisms of transport in tandem: diffusion through the matrix and seepage through the nanotube system [52].

3.2.1. Gas flow within the nanotube

Mass conservation of gas within the nanotube assembly is [53]:

$$\frac{\partial m_n}{\partial t}+\nabla\left(\rho_g\vec{\mu}\right)=Q_{sn} \tag{6}$$

where ρ_g is the density of the free-phase gas, kg/m^3, $\vec{\mu}$ is the Darcy velocity vector, m/s, Q_{sn} is the gas source (or sink), kg/(m^3*s), m is the gas content, (kg/m^3) and only free gas exits from the nanotube. According to the ideal gas law, m_n is [53]:

$$m_n=\frac{Mg}{RT}p_n\phi_n \tag{7}$$

where M_g is the molecular mass of the gas, kg/mol, R is the universal gas constant, J/mol/K, and T is the absolute gas temperature, K.

Assuming that the effect of gravity is relatively small and can be neglected, the Darcy velocity, $\vec{\mu}$, is given by:

$$\vec{\mu}=-\frac{k_n}{\mu}\nabla p_n \tag{8}$$

where k_n is the permeability of the nanotube, m^2, μ is the dynamic viscosity of the gas, Pa*s., and ∇p_n is the fluid pressure gradient, Pa/m. Due to the gas slippage effect, a modified Darcy flow is applied in order to calculate the velocity as:

$$\vec{\mu}=-\frac{k_{apn}}{\mu}\nabla p_n \tag{9}$$

where k_{apn} is the apparent permeability of the nanotube, m^2, which is defined as [19]:

$$k_{apn}=\left(1+\frac{4Kn}{1+Kn}\right)k_n \tag{10}$$

where Kn is the Knudsen number.

3.2.2. Gas flow within the matrix

Mass conservation of gas within the matrix is defined as:

$$\frac{\partial m_m}{\partial t}+\nabla\cdot J_m=Q_{sm} \tag{11}$$

where J_m is the mass flux in the matrix, kg/(m^2*s), Q_{sm} is the mass source term, kg/(m^3*s), and m_m is the gas mass in the matrix, which contains both free gas and adsorbed gas as [54]:

$$m_m=\rho_g\phi_m+\rho_{ga}\rho_{sh}\frac{p_m V_L}{p_m+P_L} \tag{12}$$

where ρ_g is the density of the free-phase gas, kg/m^3, ϕ_m is the porosity of the matrix, ρ_{ga} is the density of the gas at standard state, kg/m^3, ρ_{sh} is the density of the shale, kg/m^3, p_m is the gas pressure in the matrix, Pa, V_L is the Langmuir volume constant, m^3/kg, and P_L is the Langmuir pressure constant, Pa.

The mass flux (J_m) is the superposition of the effective diffusion and the gas mass and is defined as [7]:

$$J_m=-De\nabla m_m \tag{13}$$

where D_e is the effective diffusion coefficient, m^2/s.

The diffusion process is dominated by random molecular motion and is described by the effective diffusion coefficient, D_e. The effective diffusivity includes both bulk diffusion and Knudsen diffusion. The diffusion coefficient for Knudsen diffusion is expressed as [55]:

$$D_m=\frac{1}{3}u_m d_m \tag{14}$$

where d_m is the pore diameter in the matrix inclusions, m, and u_m is the arithmetic average of the gas velocity, m/s [56]:

$$u_m=\sqrt{\frac{8RT}{\pi M_g}} \tag{15}$$

When considering the effect of porosity, tortuosity, and roughness, Eq. (14). becomes [57,58]:

$$D_m^e=\frac{\phi_m}{\tau_m}(\psi)^{D_f-2}D_m \tag{16}$$

where D_f is a dimensionless constant that represents the fractal dimension of the pore wall, ψ is also a dimensionless number that is defined as the ratio of the gas-molecule diameter and the local average pore diameter, and ϕ_m and τ_m are the porosity and tortuosity of the matrix, respectively.

For a single pure gas with self-diffusion, the bulk diffusion coefficient can be obtained from molecular kinetic theory as [55]:

$$D_b = KnD_m \tag{17}$$

Considering the effect of porosity and tortuosity, Eq. (17) becomes [61,62]:

$$D_b^e = \frac{\phi_m}{\tau_m} KnD_m \tag{18}$$

Dongari [55] proposed a general way of calculating the effective diffusion coefficient as:

$$D_{ef}^e = \left(\left(D_m^e\right)^\zeta + \left(D_b^e\right)^\zeta \right)^{\frac{1}{\zeta}} \tag{19}$$

where ζ is the interpolation constant. In the case of $\zeta = -1$, effective diffusion becomes either Knudsen diffusion or bulk diffusion when $Kn > 10$ or $Kn < 0.01$ [55]. Thus $\zeta = -1$ is applied in the present work.

3.3. Permeability model

Permeability varies with porosity as [59]:

$$\frac{k}{k_0} = \left(\frac{\phi}{\phi_0}\right)^3 \tag{20}$$

where k is permeability, m^2, ϕ is porosity, and the subscript 0 denotes the initial value of the variable.

In the present work, constant confining pressure conditions are chosen as representative boundary conditions for the system, and the representative unit is free to swell or deform. In the initial stage, matrix swelling is confined to the vicinity of the nanotube compartment and the total volume of the REV does not change. Porosity can be expressed as Eq. (21). As gas continues to enter into the matrix, the swelling zone propagates further into the matrix and it becomes global swelling. In the global swelling stage, the total volume changes. The expression for porosity is Eq. (22).

$$\phi_l = \pi(r_{n0} + \Delta rn)^2 / \pi rm0^2 = \left(\frac{r_{n0} + \Delta rn}{r_{m0}}\right)^2 \tag{21}$$

$$\phi_g = \pi(r_{n0} + \Delta rn)^2 / \pi(r_{m0} + \Delta rm)^2 = \left(\frac{r_{n0} + \Delta rn}{rm0 + \Delta rm}\right)^2 \tag{22}$$

where ϕ_l and ϕ_g are the porosities of shale after local deformation and overall deformation, respectively.

The porosity ratio then evolves with nanotube strain and volume strain as:

$$\frac{\phi_l}{\phi_0} = (1 + \Delta rn / r_{n0})^2 = 1 + \varepsilon_{fs} \tag{23}$$

$$\frac{\phi_g}{\phi_0} = (1 + \Delta rn / r_{n0})^2 \left(1 / \left(1 + \frac{\Delta rm}{r_{m0}}\right)\right)^2 = \frac{1 + \varepsilon_{fs}}{1 + \varepsilon_{vs}} \tag{24}$$

In this approach, permeability evolution is dominated by the ratio of the nanotube strain and volume strain instead of by the nanotube radius/aperture, the latter of which has been the case in previous work [7].

4. Verification with experimental data

In the present section, the fully coupled model is implemented in – and solved with COMSOL Multiphysics. Specifically, two representative experimental profiles are employed in order to verify the coupled model. The procedure and results of the model validation are reported in the following.

4.1. Experimental phenomena

We use results for gas injection and adsorption on an intact sample of Barnett shale under constant confining pressure conditions [11]. The sample in the experiment was cylindrical with a diameter of 3.81 cm and a length of 7.62 cm. The pressure pulse decay test method was employed in order to assess shale permeability with a constant confining pressure of 15 MPa with permeability observed to monotonically decrease. A second and separate experiment measured the gas permeability of Bossier shale under constant confining pressure conditions [15]. The sample was again cylindrical with a diameter of 38.3 mm and a length of 12.4 mm. The gas pressure was gradually increased from 0.15 MPa to 12 MPa while the surrounding pressure was held at 12 MPa. In this experiment, a non-steady-state method was used to measure permeability with permeability first decreasing and then recovering slightly, in contrast to the previous experiments [11].

4.2. Model set-up

The following validation prescribes three main assumptions: (i) The shale sample is assumed to consist of nanotube and matrix units, (ii) a unit representative of the permeability variation across the sample can be found, and (iii) the effect of boundary conditions on the sample has the same effect on the representative unit.

For the geometric model, the nanotubes are embedded in the matrix as long cylinders and form a complete separation between the matrix blocks, as shown in Fig. 1 (c). We characterise the organic and inorganic composition of the shale matrix using a Monte Carlo stochastic method [60,61], as shown in Fig. 4 (a). Details of the algorithm can be found in the respective articles [60,61]. As can be seen from the figure, the nanotubes are located in the inorganic matrix, and the organic matter is randomly distributed around the nanotubes. In order to simplify the

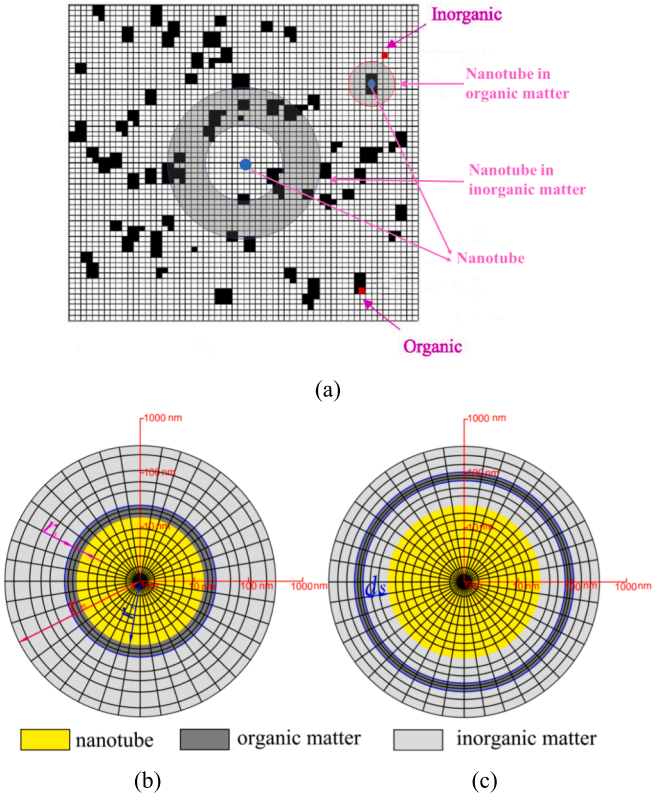

Fig. 4. (a): The distribution of organic and inorganic components of the shale matrix [60]; The positioning of nanotubes within shale: (b) nanotube in organic matter; (c) nanotube in inorganic matter.

calculations and reduce the computational effort, the discrete distribution of organic matter around the nanotubes is combined into a single ring of organic matter. A nanotube-inorganic–organic-inorganic multilayer nested model was developed. The distance from the single ring of organic matter to the nanotube wall refers to the thickness of inorganic matrix denoting the proportion of inorganic matrix. Since the nanotube length is large compared to the radius, a two-dimensional plane strain model is employed, as shown in Fig. 4 (b-c). As mentioned above, two types of nanotubes are present in the shale matrix – that is, in either organic or inorganic matter – and are simulated as shown in Fig. 4 (b) and (c), respectively. The geometric dimensions are shown in Fig. 4 on logarithmic axes.

The "sweep" feature was employed in COMSOL Multiphysics in order to mesh the geometric model. For Fig. 4 (b), there are 1,700 domain elements and 468 edge elements for the full mesh, with 2,320 domain elements and 496 edge elements for Fig. 4 (c). In order to achieve the coupling process, the Darcy's Law module and the solid mechanics module are employed to implement Eqs. (6) and (11) and Eqs. (3) and (4), respectively. Injection of the adsorbed gas was investigated with the injection pressure applied at the centre of the nanotube. For the mechanical model, the boundary condition is given as:

$$\sigma \cdot n = p \tag{25}$$

for the constant confining pressure condition.

For the gas flow boundary model, the flow boundary condition is given as:

$$p_n = p_m \tag{26}$$

for the interface between the nanotube and the matrix.

4.3. Fitting results

This nanotube-in-organic-matter model (Fig. 4 (b)) is employed to match the experimental results of Shen's work since most nanotubes were observed in the organic matter in the Barnett shale [36]. Conversely, the nanotube-in-inorganic-matter model of Fig. 4 (c) is used to represent Fink's work because in this sample the nanotubes were mainly distributed within the inorganic matter [62]. For the simulation model, the injection pressure (P_{in}) is applied to the interior boundary of the nanotube system, and no flow boundary conditions are applied to the other boundaries. The confining pressure is applied to all external boundaries and held constant. The input parameters for the simulation model are listed in Table 1 [11,15,63,64]. As shown in Fig. 5, the modelling results are in good agreement with the experimental observations. Fig. 5(a) and (b) have a degree of fit of $R^2 = 0.94$ and 0.93, respectively. The effect of simulated gas pressure on permeability did not begin from the initial state, mainly because the increasing phase was difficult to capture experimentally due to the high transport capacity of the nanotube.

4.4. Discussion of matching results

With the permeability–gas pressure profile analysed in Fig. 5, permeability evolution with time is shown in Fig. 6 with two different three-stage permeability profiles displayed. Fig. 6 (a) shows permeability first increasing, then decreasing, and finally, equilibrating. Fig. 6 (b) displays a different trend, with permeability first increasing, then decreasing to a minimum value, and finally, recovering slightly.

As mentioned previously, permeability evolves as the result of a transition from local to global behaviour. The increase in permeability at early time (stage) is a result of both the increase in gas pressure in the nanotubes and the local swelling of the nanotubes. The decrease in permeability mainly results from the increased gas pressure and gas adsorption behaviour as the gas diffuses into the shale matrix. As the gas pressure propagates further, global swelling increases both the volume of the shale matrix and the aperture of the nanotube. The differences between these two permeability profiles are apparent in the last stage (late time) either as a continuous decrease or as a slight recovery in permeability. The reason for the discrepancy depends on the competition between the local swelling of the nanotube and the global swelling of the matrix, with the former component increasing permeability and the latter decreasing the permeability. When the global swelling dominates permeability evolution in the last stage, permeability continues to decrease, as shown in Fig. 6 (a). While the local swelling of the nanotubes dominates permeability evolution, a recovery stage appears (Fig. 6 (b)). As illustrated in this case, the location of the nanotube may have been one reason for this discrepancy, and the equilibrium permeability value was lower than the maximum value obtained in the increasing stage.

Table 1
Parameters of the simulation model for model verification.

Parameter	Meaning	Value	
		Shen	Fink
General parameters from the literature [63,64]:			
ρ_{sh}	Shale density	2,600 [kg/m^3]	2,600 [kg/m^3]
ρ_{ga}	Gas density at standard pressure	0.717 [kg/m^3]	0.717 [kg/m^3]
ν	Poisson's ratio	0.33	0.33
R	Molecular gas constant	8.3 [J/(mol*K)]	8.3 [J/(mol*K)]
T	Temperature	300 [K]	300 [K]
Mg	Molar mass of gas	0.016 [kg/mol]	0.016 [kg/mol]
Experimental conditions collected from Shen [11] and Fink [15]:			
k_{n0}	Nanotube permeability	1.28×10^{-19} [m^2]	3.3×10^{-19} [m^2]
μ	Viscosity	1.78×10^{-5} [Pa*s]	1.78×10^{-5}[Pa*s]
Parameters assumed in the present work:			
r_n	Nanotube radius	30 [nm]	40 [nm]
r_m	Matrix length	500 [nm]	500 [nm]
r_s	Organic thickness	30 [nm]	50 [nm]
	Nanotube location	Organic matter	Inorganic matter
ε_L	Langmuir strain constant	0.07	0.05
V_L	Langmuir volume constant	0.0322 [m^3/kg]	0.0322 [m^3/kg]
P_L	Langmuir pressure constant	1.5 [MPa]	1 [MPa]
ζ	Interpolation constant	–1	–1

5. Results and discussion

We conduct a parametric study to constrain controls on permeability evolution under different geological conditions - input parameters are as listed in Table 2 [64–67].

5.1. Impact of nanotube radius on permeability

The phenomenology of nanotubes embedded in organic matter (Fig. 4 (b)) is employed to investigate the effects of varying nanotube radii (i.e. 25 nm, 30 nm, 35 m, 40 nm) on permeability evolution (Fig. 7 (b)), which can be correspond to different pores diameters in shale. A significant change in permeability evolves for the case of a small radius with all scenarios exhibiting two stages: first an increase and then a decrease.

In order to further determine the impact of the radius on permeability evolution, the variation in the nanotube radius for the case of r_n = 40 nm is displayed in Fig. 7 (a). Unlike with permeability evolution, three stages were exhibited: (1) An increase in the nanotube radius: At the beginning of the gas injection phase, as the gas pressure in the nanotube increases while the gas pressure in the matrix remains constant, the pressure difference results in a local strain in the nanotube, matrix shrinkage and an increase in the nanotube radius. (2) A decrease in the nanotube radius: During this stage, the matrix pressure increases as gas is adsorbed and diffuses into the matrix. Gas adsorption results in local strain in the matrix and to a decrease in the nanotube radius. (3) An

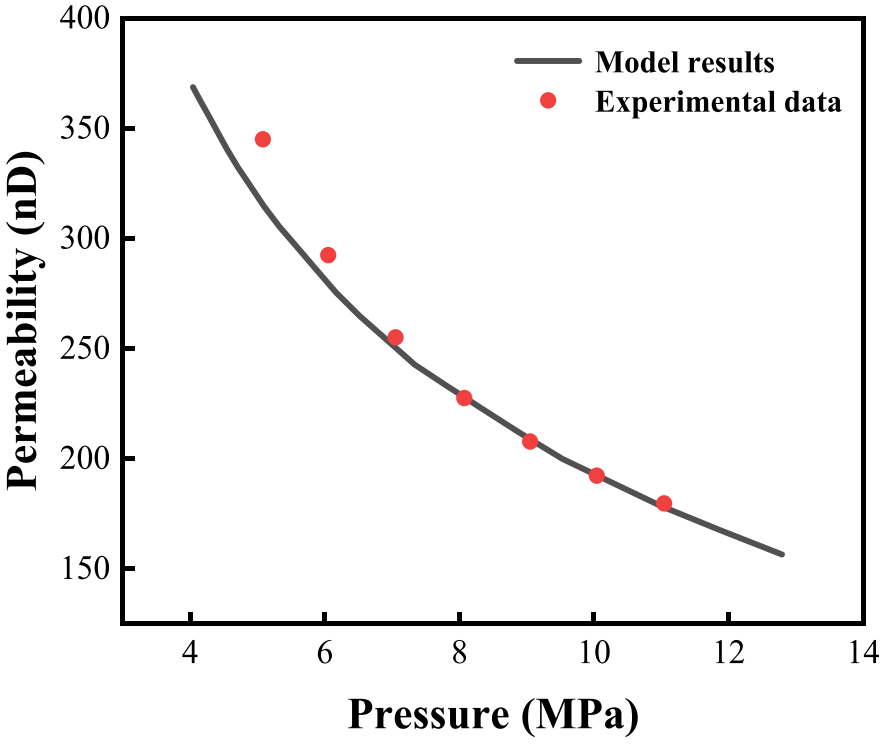

(a)

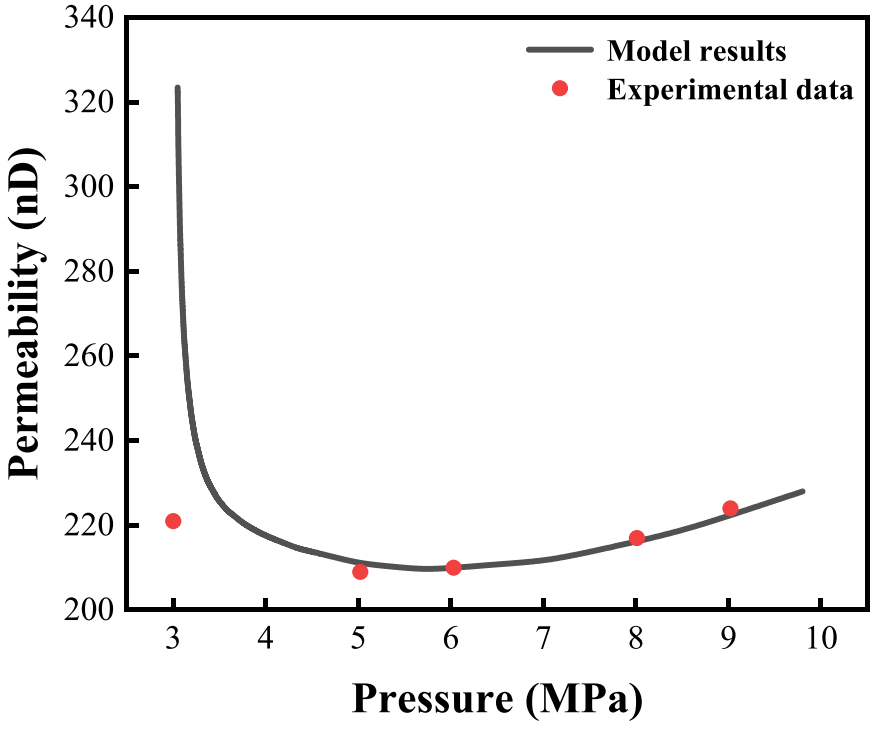

(b)

Fig. 5. Comparisons of calculated permeability with experimental data in (a) Shen et al.'s work [11] and (b) Fink et al.'s work [15].

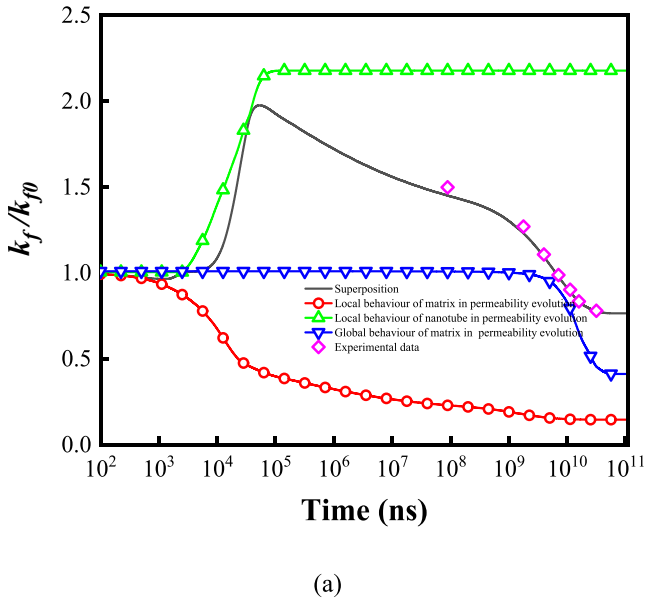

(a)

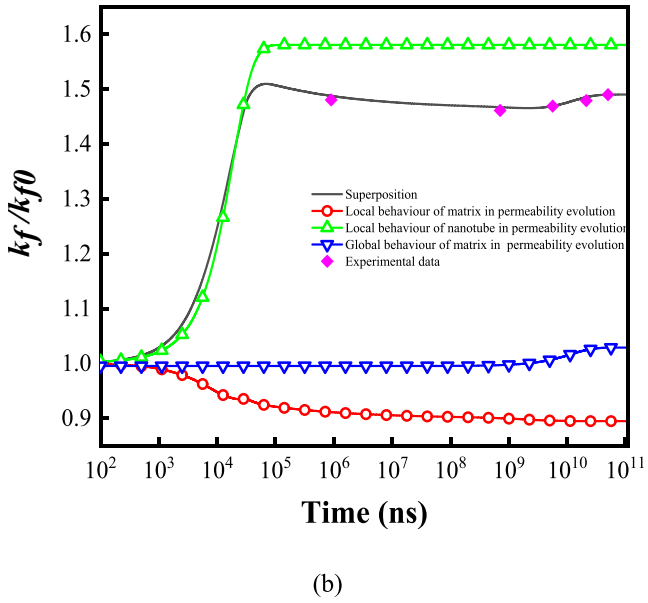

(b)

Fig. 6. Contributions of different behaviours to shale permeability: (a) decrease in permeability and (b) recover in permeability under constant confining pressure.

Table 2
Parameters of the numerical model.

Parameter		Value
General parameters from the literature [65]:		
ϕ_{f0}	Initial porosity of the nanotube	0.0064
k_{f0}	Initial permeability of the nanotube	4×10^{-17} [m^2]
ε_L	Langmuir strain constant	0.05
V_L	Langmuir volume constant	0.0322 [m^3/kg]
P_L	Langmuir pressure constant	1.5 [MPa]
Parameters assumed in the present work:		
r_m	Matrix length	500 [nm]
r_n	Nanotube radius	40 [nm]
d_s	Distance between organic matter and nanotube	10 [nm]
r_s	Organic thickness	30 [nm]

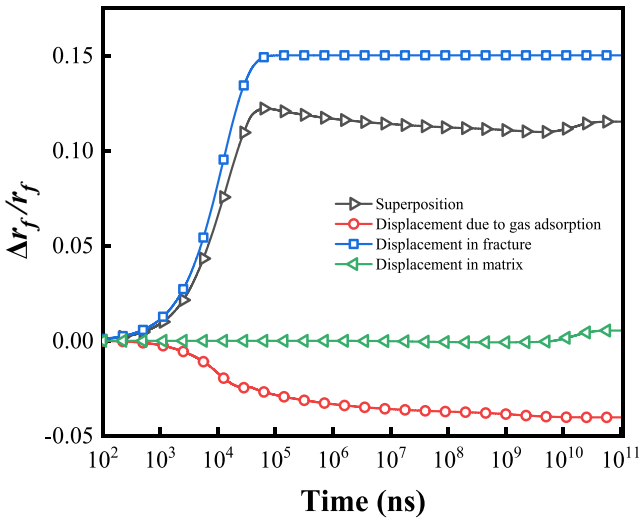

(a)

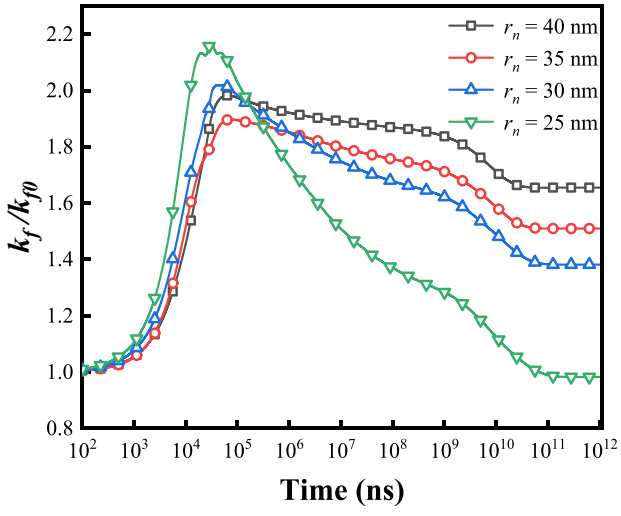

(b)

Fig. 7. Evolution of (a) permeability and (b) nanotube radius for adsorbing gas (CH4) under constant confining pressure.

increase in the nanotube radius: As the gas diffuses further into the matrix, the volume of gas adsorption and swelling increases further until the gas fills the entire control volume. As the control volume swells under constant confining pressure conditions, the nanotube also swells, and the nanotube radius increases. In this stage, permeability continues to decrease because the outward swelling of the shale matrix is greater than the local swelling of the nanotube due to its smaller geometric size, which results in reduced porosity and thus also to lower permeability. Therefore, in the case of constant confining pressure, permeability evolution could not be represented by the variation in nanotube aperture due to the increased total volume. As the porosity is usually ultra-low in the shale matrix, a decrease in permeability is frequently observed in experiments, but recovery is rarely observed.

5.2. *Impact of Young's modulus*

The shale matrix contains various minerals that exhibit different mechanical properties [68], with the Young's modulus of the inorganic matrix is usually larger than that of the organic matrix [69], reflecting

the heterogeneity of the mechanical properties of the shale matrix. Three different distributions of moduli – that is, convex, concave and linear – were assigned in order to investigate the impact of a non-homogeneous distribution of the Young's modulus. As Fig. 8 illustrates, the permeability profile behaves similarly with varying distribution, while a significant difference was observed for the maximum and minimum values. The smallest permeability appears for the case of the convex distribution, with the largest appearing in the case of the linear distribution. Moreover, for lower permeability, the nanotube aperture continued to decrease, with no recovery stage for the aperture apparent.

In order to investigate the reasons for the dramatic decline in permeability for the convex functional form, we examined the evolution of the changing ratio of nanotube radius ($\Delta r_n/ r_n$) and matrix radius ($\Delta r_m/ r_m$), as shown in Fig. 9. In the early stages, the effect of local strain on the nanotubes is enhanced due to the lower Young's modulus in the case of a convex distribution, which led to a significant increase in permeability. However, in the later stage, a relatively small discrepancy was found for three scenarios because the differences among the Young's moduli became smaller, and a significant decrease was found for the convex distribution. At the same time, in the final stage, the nanotubes no longer swell due to constraint of shale matrix boundary. This phenomenon is mainly due to the rapid increase in Young's modulus at the shale matrix boundary, which transforms the constant confining pressure boundary condition into a constant volume boundary condition as the global expansion of the matrix is reduced. Under this condition, the swelling strain that had been caused by matrix local adsorption dominates the variation of the nanotube radius instead of the global swelling.

5.3. Impact of adsorption strain

High maturity of organic matter often results in a larger gas sorption capacity [70,71] with the adsorption strain linearly proportional to this gas adsorption capacity [72]. The geometric model of Fig. 4 (b) is adopted in order to investigate the impact of adsorption strain on permeability evolution. Fig. 10 illustrates the evolution of nanotube permeability for different adsorption strains, with the same trend of permeability evolution is obtained. The equilibrium permeability ratios all decrease with increasing adsorption strain. As the matrix undergoes local swelling in the early stage, a more pronounced reduction is observed in nanotube aperture for the case of greater adsorption strain.

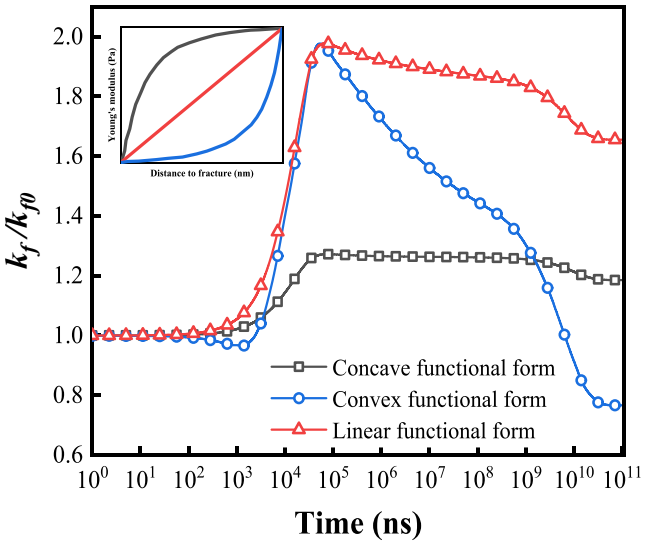

Fig. 8. Permeability evolution for the heterogeneous distribution of the Young's modulus under constant confining pressure.

However, in the global swelling term in the later stage, higher adsorption strain leads to a significant increase in matrix radius, as shown in Fig. 11. However, the adsorption strain has little effect on the appearance of the permeability recovery stage because the adsorption strain increases the nanotube aperture as the local strain and increases the matrix radius as the global strain, while the changing ratio of nanotube radius/aperture is lower than that of the matrix radius in the later stage.

5.4. Impact of organic matter content

The effect of varying organic radius/thickness on permeability evolution was numerically simulated using the geometric model shown in Fig. 4 (b). For a fixed volume, the variation in organic matter thickness represents the amount of organic matter in the shale matrix. Fig. 12 illustrates the results, and two different trends in permeability profiles are observed: (i) Permeability first increases, then decreases, and finally, remains constant, and (ii) permeability first increases, but as the gas enters the matrix, permeability recovers slightly when global behaviour evolves, and then remains constant. As the organic matter radius/thickness decreases, the final equilibrium permeability ratio also gradually decreases. When the thickness of the organic matter is sufficiently large, permeability recovery occurs in the global behaviour stage. In order to investigate the reason for the recovery in permeability, in Fig. 13, we examine the effect of organic matter radius/thickness on the radius ratio of the nanotubes and the matrix. The global swelling of the matrix is the main contributor to the recovery in nanotube radius. Conversely, permeability evolution in the last stage is as a result of the competing effects of the matrix volume strain and the nanotube strain. As the thickness of the organic matrix increases, the strain in the nanotubes becomes more pronounced at late time, and the impact of the matrix volume strain in this stage reduces, as shown in Fig. 13. The recovery of permeability is the result of strain in the nanotubes, which dominates the global behaviour as the radius/thickness of the organic material increases.

5.5. Impact of nanotube type

Previous work has focused on nanotubes embedded in organic matter – we now focus on nanotubes located within inorganic matter – for the geometry of Fig. 4. (c). Fig. 14 illustrates permeability evolution with different separation distances of the organic matter to the nanotube wall. The distance between nanotubes and organic matter can be interpreted as the positioning of nanotubes within the inorganic matrix. Equivalently, this concept can be understood as reflecting the heterogeneity of pores in shale. Two different trends are apparent: The permeability reveals a recovery phase as the organic matter is placed farther away from the nanotubes, with a gradually increase in final permeability. With the nanotubes in the inorganic matter, the initial phase of gas injection simply causes a change in effective stress, which leads to an increase in permeability. As the organic matter is situated farther away from the nanotube wall, the compression effect due to matrix adsorption swelling decreases. At the same time, however, the increase in distance both enhances the contribution of the global deformation to the increase in nanotube radius and decreases the change in matrix volume, as shown in Fig. 15. The nanotube strain increases at a more rapid rate than the volumetric strain and dominates permeability evolution - the main reason why permeability increases.

5.6. Discussion

5.6.1. Why permeability varies in the final stage?

Results from a large number of experimental observations were synthesized in order to examine permeability evolution under constant confining pressure [12,73,74]. The permeability profiles exhibit two different trends in the final stage: (1) a further decrease in permeability [11,12] and (2) a slight recovery in permeability [14,15]. In order to

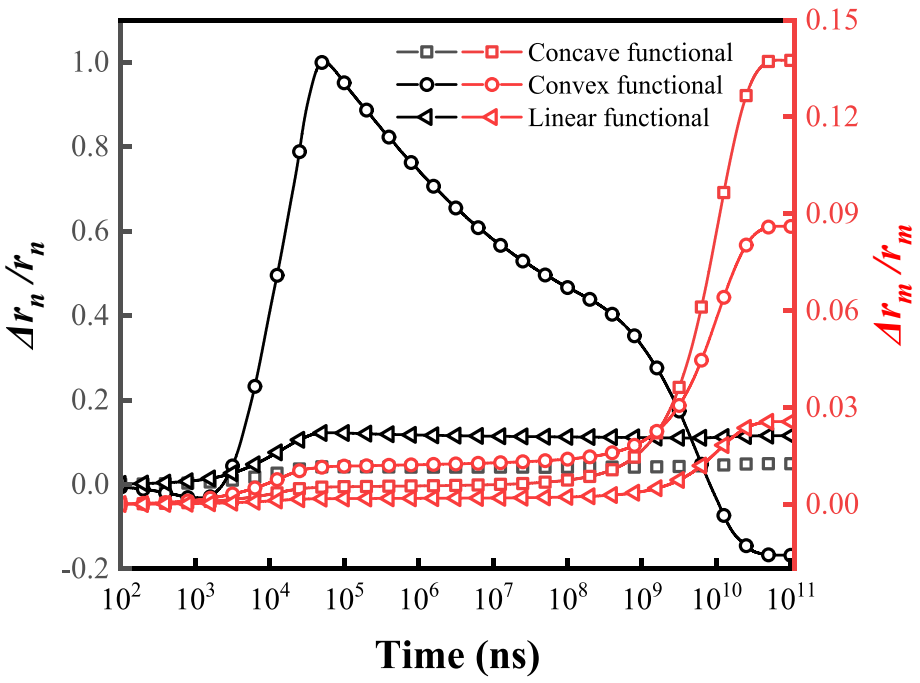

Fig. 9. Evolution of the nanotube radius ratio and the matrix radius ratio for a heterogeneous distribution of the Young's modulus under constant confining pressure.

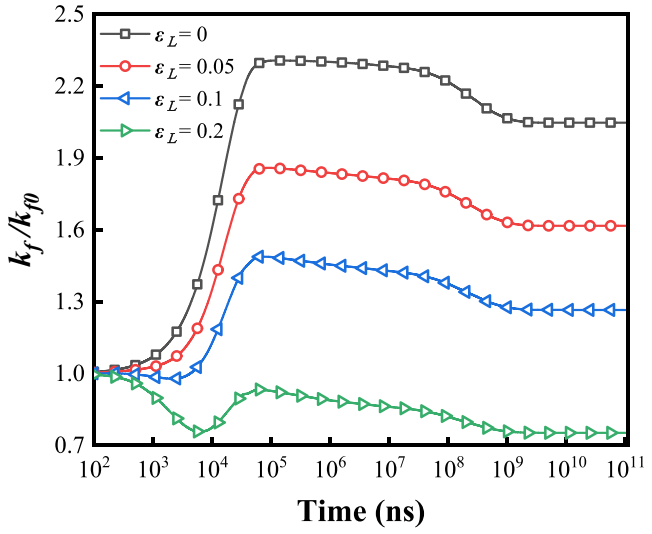

Fig. 10. Influences of adsorption strain on permeability evolution under constant confining pressure.

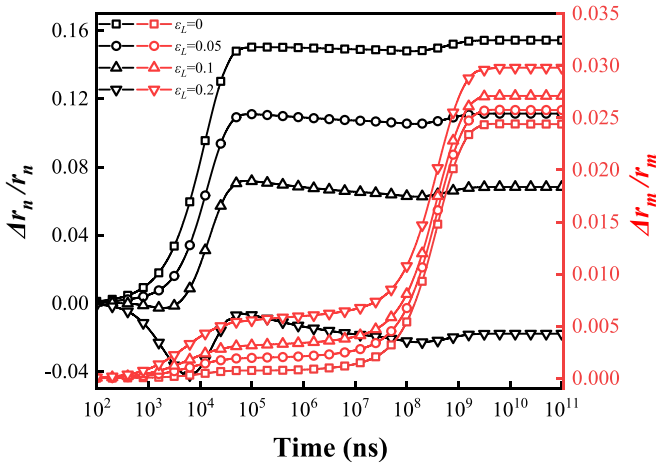

Fig. 11. Influences of adsorption strain on nanotube radius ratio and matrix radius ratio evolution under constant confining pressure.

determine the reasons for this enigmatic response, we propose this multi-layer nanocased model and find that permeability evolution in the late stages of injection is determined by both the strain of the nanotube and the global strain of the matrix. The former term increases permeability and the latter term decreases permeability in the last stage. When the matrix volume strain dominates, permeability continues to decrease in the last stage. Conversely, when the strain in the nanotubes is dominant, permeability rebounds in the last stage. This is the reason why permeability evolution exhibits two different forms in the final stage.

In various theoretical studies [75–77], the recovery stage can be clearly observed, which is barely discernible in our new model. However, the permeability recovery stage in our models is inconsistent with experimental observations, in which the final permeability ratio has generally been greater than unity because only local deformation, that induced by nanotube swelling, has been considered in these previous models. Also, reasons why the recovery stage is rarely observed have also been given: (i) The global swelling of the matrix has been found to reduce the enhancement effect caused by the local swelling of nanotubes, (ii) a specific condition has been required for the appearance of the recovery stage, such as the cases of nanotubes in inorganic matter with a certain distance to the organic matter or in high content-organic matter, and (iii) even though a recovery stage may have appeared, it occurs at very late time since diffusion within the matrix is several orders of magnitude slower than that for flow within the nanotubes.

5.6.2. *Impact of pore heterogeneity on permeability evolution*

Shale matrix exhibits high heterogeneity that comprises both organic and inorganic matter [68]. For the majority of shale gas reservoirs, nanotubes are concentrated within the organic matter, with relatively fewer existing in the inorganic matrix [60]. Parameter sensitivity studies explore this feature in order to investigate the impact of pore heterogeneity on permeability evolution. When the nanotube is located in the

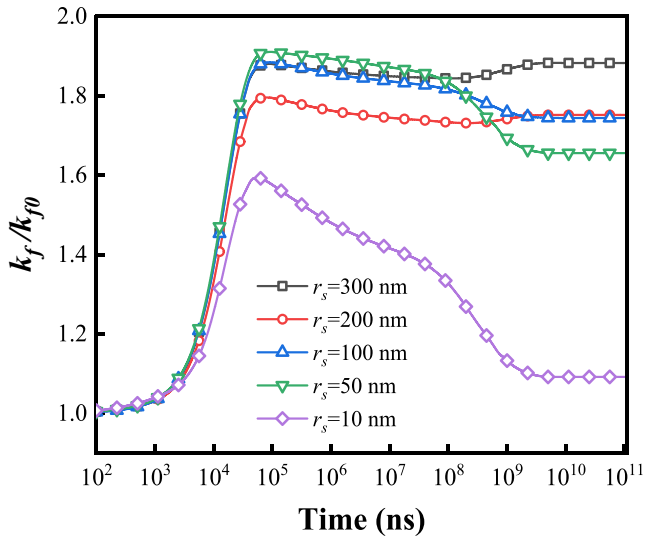

Fig. 12. Influences of organic matter thickness on permeability evolution under constant confining pressure.

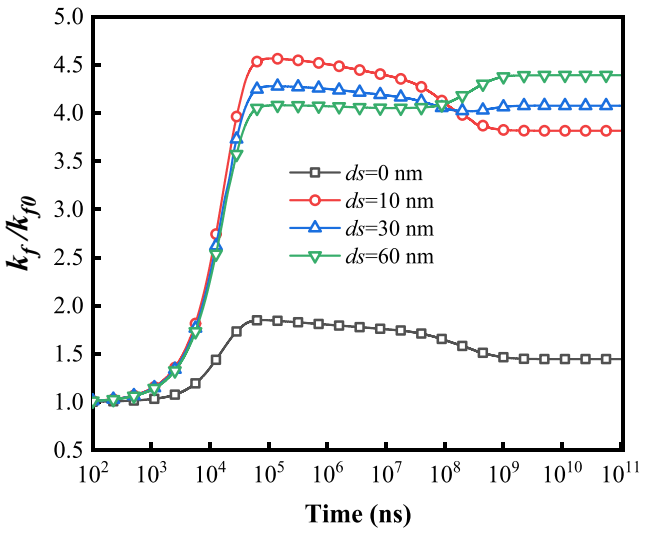

Fig. 14. Effect of nanotube type on permeability evolution under constant confining pressure.

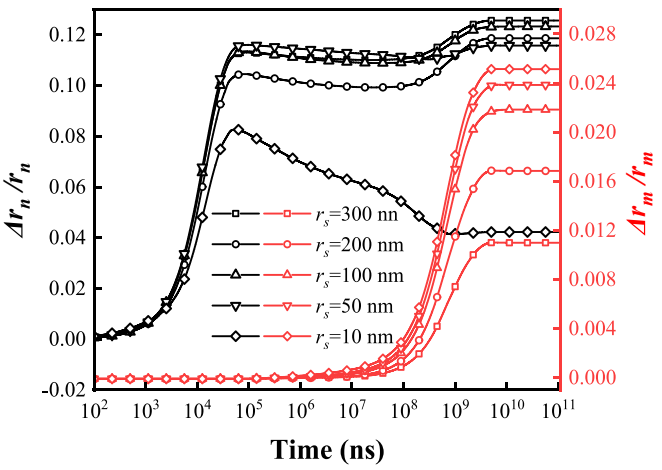

Fig. 13. Influences of organic matter thickness on the evolution of radius ratio under constant confining pressure.

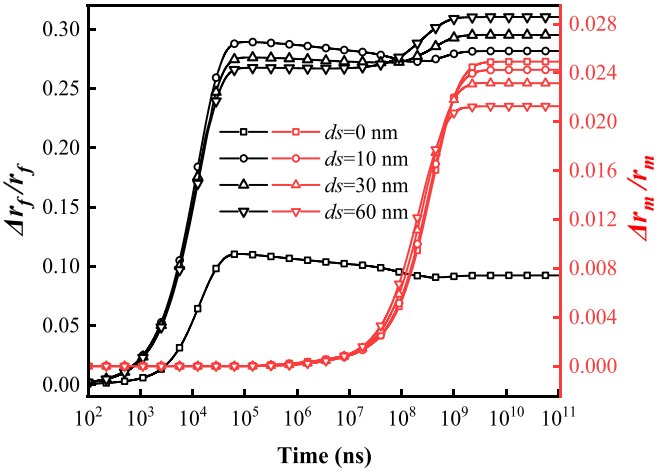

Fig. 15. Effect of nanotube type on radius ratio evolution under constant confining pressure.

organic matter, (i) a smaller nanotube radius (i.e. lower permeability) often results in a significant variation in permeability, (ii) a lower Young's modulus and larger adsorption strain results in significant local strain in the nanotube and therefore also in a dramatic decrease in the permeability, and (iii) when the adsorption layer is sufficiently large, a recovery stage appears. For the scenario of the inorganic nanotube, the permeability is found to increase in most cases, which is consistent with classical effective stress theory.

These observations illuminate mechanisms of importance in shale gas exploitation and CO_2 geological storage. The ultra-low porosity of the shale matrix leads to a significant variation in permeability during the gas injection and depletion processes. For reservoirs with high total organic content (TOC), the global strain of the shale matrix dominates the permeability evolution, with permeability decreasing during gas injection and increasing during gas depletion. Conversely, for the nanotube in the inorganic matrix, the permeability evolution follows classical effective stress theory.

5.6.3. *Comparisons with previous work*

Recently, a number of literatures [5,7,14,15] are conducted to address the permeability evolution with increasing pore pressure under constant confining pressure. In the previous work [7], a simple topological structure - a small circle embedded into a big circle or a small rectangle embedded into a big square was employed. In this work, a multi-layer nanocased topological structure is proposed based on the distribution characteristic of organic matter obtained from Monte Carlo method. In this approach, the interactions between different components and its impact on the permeability evolution can be fully addressed.

Unlike the previous work [29,30], both the local nanotube strain and global matrix strain are considered in the current work. The permeability evolution especially in the last stage is determined by the competition between these two strains. The former term enhances the permeability with the latter term decreasing the permeability during the gas injection process. With these two strains considered simultaneously, the final permeability ratio is more likely to conform to empirical data in contrast to earlier models [7,76] where it frequently exceeded one violating the experiment observations.

6. Conclusions

The transient responses of shale permeability to temporal and spatial variations due to matrix-nanotube interactions under stress-controlled conditions are explored. A multi-layer nanocased model is proposed in

order to replicate observed permeability evolution profiles. This model comprises a central cylindrical nanotube representing the pore and surrounded by a cylindrical sorbing shale sheath (nanocase) that is free to swell and deform poro-elastically. Deformations of the pore and substrate are used to follow the evolution of an equivalent permeability of the composite pore-shale system. A parameter sensitivity test is conducted in order to investigate the effect of pore heterogeneity on permeability evolution. Based on the results of the model, the following conclusions are drawn:

(1) The classical nanotube-matrix interaction-based permeability model requires correction. At constant confining pressure, the permeability evolution cannot be expressed purely in terms of nanotube aperture because the total volume has increased. Matrix radius is considered in the model, and the permeability evolution is found to be the result of a combination of local strain on the nanotubes and global strain on the matrix, which can adequately explain why the final permeability ratio is not experimentally greater than one.
(2) The reason that permeability behaves differently in the final stage – that is, by either continuing to decrease or recovering – is given. The global swelling of the sorbing shale decreases the porosity and therefore the permeability. Conversely, the local strain of the nanotube increases the nanotube aperture and thus increases the permeability. When global swelling dominates, permeability continues to decrease in the last stage; otherwise, a recovery stage appears in the permeability profile.
(3) The phenomenon whereby the recovery stage in permeability evolution is rarely observed is explained. In most shale reservoirs, the geometric size of the shale matrix (radius) is significantly larger than that of the nanotube, and therefore, global swelling has dominated the permeability evolution in the last stage. The permeability recovery stage has only been observed in the case of larger organic content, and it only appears at very late time – requiring a long observation period for its appearance.
(4) The impact of pore heterogeneity on permeability evolution is examined. Smaller nanotube radii or lower porosity lead to greater variation in permeability. Moreover, a smaller Young's modulus or a larger adsorption strain (high maturity) result in a significant decrease in permeability. When the nanotube is located in an inorganic matrix, permeability evolution follows the response dicated by classical effective stress theory.

CRediT authorship contribution statement

Wangxing Cheng: Writing – original draft, Software, Data curation. **Guanglei Cui:** Writing – review & editing, Conceptualization. **Yuling Tan:** Methodology. **Derek Elsworth:** Validation, Supervision. **Chunguang Wang:** Funding acquisition. **Chengxiang Yang:** Funding acquisition. **Tianyu Chen:** Funding acquisition. **Chuanzhong Jiang:** Methodology.

Declaration of competing interest

The authors declare that they have no known competing financial interests or personal relationships that could have appeared to influence the work reported in this paper.

Data availability

Data will be made available on request.

Acknowledgment

This work is a partial result of funding by the National Key Research and Development Program of China (No. 2021YFC2902101), National Natural Science Foundation of China (Grant No. 12002081), and the "111" Project (Grant No. B17009). DE gratefully acknowledges support from the G. Albert Shoemaker endowment.

References

[1] Doe U. Annual energy outlook 2016 with projections to 2040. (No. DOE/EIA0383 (2016)). Washington, DC (United States): USDOE Energy Information Administration (EI); 2016 [Office of Energy Analysis].
[2] Cui G, Liu J, Wei M, Feng X, Elsworth D. Evolution of permeability during the process of shale gas extraction. J Nat Gas Sci Eng 2018;49:94–109.
[3] Peng Y, Liu J, Pan Z, Connell LD. A sequential model of shale gas transport under the influence of fully coupled multiple processes. J Nat Gas Sci Eng 2015;27:808–21.
[4] Cao P, Liu J, Leong Y-K. Combined impact of flow regimes and effective stress on the evolution of shale apparent permeability. J Unconv Oil Gas Resour 2016;14:32–43.
[5] Moghadam AA, Chalaturnyk R. Laboratory investigation of shale permeability SPE Canada Unconventional Resources Conference. SPE 2015:SPE-175919-MS.
[6] Zhou J, Liu G, Jiang Y, Xian X, Liu Q, Zhang D, et al. Supercritical carbon dioxide fracturing in shale and the coupled effects on the permeability of fractured shale: An experimental study. J Nat Gas Sci Eng 2016;36:369–77.
[7] Cui G, Liu J, Wei M, Shi R, Elsworth D. Why shale permeability changes under variable effective stresses: new insights. Fuel 2018;213:55–71.
[8] Pan Z, Connell LD. Modelling permeability for coal reservoirs: a review of analytical models and testing data. Int J Coal Geol 2012;92:1–44.
[9] Li S, Dong M, Li Z. Measurement and revised interpretation of gas flow behavior in tight reservoir cores. J Pet Sci Eng 2009;65(1–2):81–8.
[10] Cui G, Feng X, Pan Z, Chen T, Liu J, Elsworth D, et al. Impact of shale matrix mechanical interactions on gas transport during production. J Pet Sci Eng 2020;184:106524.
[11] Shen Y, Pang Y, Shen Z, Tian Y, Ge H. Multiparameter analysis of gas transport phenomena in shale gas reservoirs: apparent permeability characterization. Sci Rep 2018;8(1):2601.
[12] Ghanizadeh A, Amann-Hildenbrand A, Gasparik M, Gensterblum Y, Krooss BM, Littke R. Experimental study of fluid transport processes in the matrix system of the European organic-rich shales: II. Posidonia Shale (Lower Toarcian, northern Germany). Int J Coal Geol 2014;123:20–33.
[13] Jin G, Pérez HG, Agrawal G, Khodja MR, Ali AZ, Hussaini SR, et al. The impact of gas adsorption and composition on unconventional shale permeability measurement. In: SPE Middle East Oil and Gas Show and Conference. SPE 2015:SPE-172744-MS.
[14] Li X, Feng Z, Han G, Elsworth D, Marone C, Saffer D, et al. Permeability evolution of propped artificial fractures in Green River shale. Rock Mech Rock Eng 2017;50:1473–85.
[15] Fink R, Krooss BM, Gensterblum Y, Amann-Hildenbrand A. Apparent permeability of gas shales–Superposition of fluid-dynamic and poro-elastic effects. Fuel 2017;199:532–50.
[16] Javadpour F. Nanopores and apparent permeability of gas flow in mudrocks (shales and siltstone). J Can Pet Technol 2009;48(08):16–21.
[17] Civan F. Effective correlation of apparent gas permeability in tight porous media. Transp Porous Media 2010;82:375–84.
[18] Klinkenberge L. The permeability of porous media to liquids and gases. Drill Prod Pract 1941:200–13.
[19] Zhang L, Li D, Li L, Lu D. Development of a new compositional model with multi-component sorption isotherm and slip flow in tight gas reservoirs. J Nat Gas Sci Eng 2014;21:1061–72.
[20] Florence FA, Rushing J, Newsham KE, Blasingame TA. Improved permeability prediction relations for low-permeability sands. In: Rocky mountain oil & gas technology symposium. OnePetro 2007 SPE-107954-MS.
[21] Javadpour F, Fisher D, Unsworth M. Nanoscale gas flow in shale gas sediments. J Can Pet Technol 2007;46(10).
[22] Brown GP, DiNardo A, Cheng GK, Sherwood TK. The flow of gases in pipes at low pressures. J Appl Phys 1946;17(10):802–13.
[23] Letham EA. Matrix permeability measurements of gas shales: gas slippage and adsorption as sources of systematic error. Undergraduate Honours Thesis. Department of Earth and Ocean Sciences. University of British Columbia; 2011.
[24] Sinha S, Braun E, Determan M, Passey Q, Leonardi S, Boros J, et al. Steady-state permeability measurements on intact shale samples at reservoir conditions-effect of stress, temperature, pressure, and type of gas. In: SPE Middle East oil and gas show and conference. SPE 2013:SPE-164263-MS.
[25] Florence FA, Rushing J, Newsham K, et al. Improved permeability prediction pe lations for low permeability sands. In: SPE 107954 rocky mountain oil & gas technology symposium held in Denver, Colorado, USA; 16–18 April 2007.
[26] Somerton WH, Söylemezoğlu I, Dudley R. Effect of stress on permeability of coal. Int J Rock Mech Min Sci Geomech Abstr. 12. Elsevier; 1975:129-45.
[27] McKee CR, Bumb AC, Koenig RA. Stress-dependent permeability and porosity of coal and other geologic formations. SPE Form Eval 1988;3(01):81–91.
[28] Pan Z, Connell LD. A theoretical model for gas adsorption-induced coal swelling. Int J Coal Geol 2007;69(4):243–52.
[29] Liu J, Wang J, Chen Z, Wang S, Elsworth D, Jiang Y. Impact of transition from local swelling to macro swelling on the evolution of coal permeability. Int J Coal Geol 2011;88(1):31–40.

[30] Wu Y, Liu J, Elsworth D, Siriwardane H, Miao X. Evolution of coal permeability: Contribution of heterogeneous swelling processes. Int J Coal Geol 2011;88(2–3):152–62.
[31] Liu J, Chen Z, Elsworth D, Miao X, Mao X. Evolution of coal permeability from stress-controlled to displacement-controlled swelling conditions. Fuel 2011;90(10):2987–97.
[32] Liu J, Chen Z, Elsworth D, Miao X, Mao X. Evaluation of stress-controlled coal swelling processes. Int J Coal Geol 2010;83(4):446–55.
[33] Guo P, Cheng Y, Jin K, Li W, Tu Q, Liu H. Impact of effective stress and matrix deformation on the coal fracture permeability. Transp Porous Media 2014;103(1):99–115.
[34] Zeng J, Liu J, Li W, Tian J, Leong YK, Elsworth D, et al. Effects of heterogeneous local swelling and multiple pore types on coal and shale permeability evolution. In: SPE Europec featured at EAGE Conference and Exhibition : SPE 2020 SPE-200587-MS.
[35] Zhou H, Zhang L, Wang X, Rong T, Wang L. Effects of matrix-fracture interaction and creep deformation on permeability evolution of deep coal. Int J Rock Mech Min Sci 2020;127:104236.
[36] Cui G, Tan Y, Chen T, Feng X-T, Elsworth D, Pan Z, et al. Multidomain two-phase flow model to study the impacts of hydraulic fracturing on shale gas production. Energy Fuels 2020;34(4):4273–88.
[37] Loucks RG, Reed RM, Ruppel SC, Jarvie DM. Morphology, genesis, and distribution of nanometer-scale pores in siliceous mudstones of the Mississippian Barnett Shale. J Sediment Res 2009;79(12):848–61.
[38] Chalmers GR, Bustin RM, Power IM. Characterization of gas shale pore systems by porosimetry, pycnometry, surface area, and field emission scanning electron microscopy/transmission electron microscopy image analyses: Examples from the Barnett, Woodford, Haynesville, Marcellus, and Doig units. Am Assoc Pet Geol Bull 2012;96(6):1099–119.
[39] Ambrose RJ, Hartman RC, Diaz-Campos M, Akkutlu IY, Sondergeld CH. New pore-scale considerations for shale gas in place calculations. In: SPE unconventional gas conference. OnePetro 2010 SPE-131772-MS.
[40] Loucks RG, Reed RM, Ruppel SC, Hammes U. Spectrum of pore types and networks in mudrocks and a descriptive classification for matrix-related mudrock pores. Am Assoc Pet Geol Bull 2012;96(6):1071–98.
[41] Tian H, Pan L, Xiao X, Wilkins RW, Meng Z, Huang B. A preliminary study on the pore characterization of Lower Silurian black shales in the Chuandong Thrust Fold Belt, southwestern China using low pressure N2 adsorption and FE-SEM methods. Mar Pet Geol 2013;48:8–19.
[42] Al Hinai A, Rezaee R, Esteban L, Labani M. Comparisons of pore size distribution: a case from the Western Australian gas shale formations. J Unconv Oil Gas Resour 2014;8:1–13.
[43] Zhou S, Yan G, Xue H, Guo W, Li X. 2D and 3D nanopore characterization of gas shale in Longmaxi formation based on FIB-SEM. Mar Pet Geol 2016;73:174–80.
[44] Zhu H, Ju Y, Lu W, Han K, Qi Y, Neupane B, et al. The characteristics and evolution of micro-nano scale pores in shales and coals. J Nanosci Nanotechnol 2017;17(9):6124–38.
[45] Vengosh A, Jackson RB, Warner N, Darrah TH, Kondash A. A critical review of the risks to water resources from unconventional shale gas development and hydraulic fracturing in the United States. Environ Sci Technol 2014;48(15):8334–48.
[46] Chen T, Feng X-T, Cui G, Tan Y, Pan Z. Experimental study of permeability change of organic-rich gas shales under high effective stress. J Nat Gas Sci Eng 2019;64:1–14.
[47] Shi M, Yu B, Xue Z, Wu J, Yuan Y. Pore characteristics of organic-rich shales with high thermal maturity: A case study of the Longmaxi gas shale reservoirs from well Yuye-1 in southeastern Chongqing. China J Nat Gas Sci Eng 2015;26:948–59.
[48] Blyverket J. Molecular dynamics modeling of clay-fluid interfaces. Thesis for the degree of Master of Science. Faculty of Mathematics and Natural Sciences. University of Oslo; 2015.
[49] Roylance D. Stress-strain curves. Cambridge: Massachusetts Institute of Technology study; 2001.
[50] Detournay E, Cheng A-H-D. Fundamentals of poroelasticity. Analysis and design methods 1993,:113–71.
[51] Cui X, Bustin RM. Volumetric strain associated with methane desorption and its impact on coalbed gas production from deep coal seams. Am Assoc Pet Geol Bull 2005;89(9):1181–202.
[52] Elsworth D, Bai M. Flow-deformation response of dual-porosity media. J Geotech Eng 1992;118(1):107–24.
[53] Zhang H, Liu J, Elsworth D. How sorption-induced matrix deformation affects gas flow in coal seams: a new FE model. Int J Rock Mech Min Sci 2008;45(8):1226–36.
[54] Saghafi A, Faiz M, Roberts D. CO2 storage and gas diffusivity properties of coals from Sydney Basin. Australia Int J Coal Geol 2007;70(1–3):240–54.
[55] Dongari N, Sharma A, Durst F. Pressure-driven diffusive gas flows in micro-channels: from the Knudsen to the continuum regimes. Microfluid Nanofluid 2009;6:679–92.
[56] Geng L, Li G, Zitha P, Tian S, Sheng M, Fan X. A diffusion–viscous flow model for simulating shale gas transport in nano-pores. Fuel 2016;181:887–94.
[57] Miao Y, Li X, Zhou Y, Lee J, Sun Z, Chang Y, et al. A new rate-transient analysis model for shale gas reservoirs coupled the effect of slip flow and surface diffusion. Int J Heat Mass Transfer 2018;124:1–10.
[58] Darabi H, Ettehad A, Javadpour F, Sepehrnoori K. Gas flow in ultra-tight shale strata. J Fluid Mech 2012;710:641–58.
[59] Chilingar GV. Relationship between porosity, permeability, and grain-size distribution of sands and sandstones. Dev Sedimentol 1964,:71–5.
[60] Zhang T, Li X, Shi J, Sun Z, Yin Y, Wu K, et al. An apparent liquid permeability model of dual-wettability nanoporous media: A case study of shale. Chem Eng Sci 2018;187:280–91.
[61] Naraghi ME, Javadpour F. A stochastic permeability model for the shale-gas systems. Int J Coal Geol 2015;140:111–24.
[62] Klaver J, Desbois G, Littke R, Urai JL. BIB-SEM characterization of pore space morphology and distribution in postmature to overmature samples from the Haynesville and Bossier Shales. Mar Pet Geol 2015;59:451–66.
[63] Guo C, Xu J, Wu K, Wei M, Liu S. Study on gas flow through nano pores of shale gas reservoirs. Fuel 2015;143:107–17.
[64] Huang T, Guo X, Chen F. Modeling transient flow behavior of a multiscale triple porosity model for shale gas reservoirs. J Nat Gas Sci Eng 2015;23:33–46.
[65] Eliyahu M, Emmanuel S, Day-Stirrat RJ, Macaulay CI. Mechanical properties of organic matter in shales mapped at the nanometer scale. Mar Pet Geol 2015;59:294–304.
[66] Chen F, Duan Y, Wang K, Li X, Liao Y. A novel pressure transient response model considering multiple migration mechanisms in shale gas reservoir. J Nat Gas Sci Eng 2015;22:321–34.
[67] Shukla P, Kumar V, Curtis M, Sondergeld CH, Rai CS. Nanoindentation studies on shales. ARMA US Rock Mechanics/Geomechanics Symposium ARMA 2013:ARMA-2013-578..
[68] Yu H, Fan J, Xia J, Liu H, Wu H. Multiscale gas transport behavior in heterogeneous shale matrix consisting of organic and inorganic nanopores. J Nat Gas Sci Eng 2020;75:103139.
[69] Sayers CM. The effect of anisotropy on the Young's moduli and Poisson's ratios of shales. Geophys Prospect 2013;61:416–26.
[70] Zhang T, Ellis GS, Ruppel SC, Milliken K, Yang R. Effect of organic-matter type and thermal maturity on methane adsorption in shale-gas systems. Org Geochem 2012;47:120–31.
[71] Huang L, Ning Z, Wang Q, Qi R, Zeng Y, Qin H, et al. Molecular simulation of adsorption behaviors of methane, carbon dioxide and their mixtures on kerogen: Effect of kerogen maturity and moisture content. Fuel 2018;211:159–72.
[72] Lin J, Ren T, Wang G, Booth P, Nemcik J. Experimental study of the adsorption-induced coal matrix swelling and its impact on ECBM. J Earth Sci 2017;28:917–25.
[73] Kang Y, Chen M, Li X, You L, Yang B. Laboratory measurement and interpretation of nonlinear gas flow in shale. Int J Mod Phys C 2015;26(06):1550063.
[74] Ren Y, Guo X, Xie C, Wu H. Experimental study on gas slippage of Marine Shale in Southern China. Petroleum 2016;2(2):171–6.
[75] Shi R, Liu J, Wei M, Elsworth D, Wang X. Mechanistic analysis of coal permeability evolution data under stress-controlled conditions. Int J Rock Mech Min Sci 2018;110:36–47.
[76] Shi R, Liu J, Wang X, Elsworth D, Wang Z, Wei M, et al. Experimental observations of gas-sorption-induced strain gradients and their implications on permeability evolution of shale. Rock Mech Rock Eng 2021;54(8):3927–43.
[77] Shi R, Liu J, Wang X, Elsworth D, Liu Z, Wei M, et al. Experimental observations of heterogeneous strains inside a dual porosity sample under the influence of gas-sorption: A case study of fractured coal. Int J Coal Geol 2020;223:103450.